Design of the submerged horizontal plate breakwater using a fully coupled hydroelastic approach

Huang, Luofeng; Li, Yuzhu

Published in:
Computer-Aided Civil and Infrastructure Engineering

Link to article, DOI:
10.1111/mice.12784

Publication date:
2022

Document Version
Peer reviewed version

Design of the submerged horizontal plate breakwater using a fully coupled hydroelastic approach

Luofeng Huang[1] | Yuzhu Li[2,3]

[1]Department of Mechanical Engineering, University College London (UCL), London, UK
[2]Department of Mechanical Engineering, Technical University of Denmark, Copenhagen, Denmark
[3]Department of Civil and Environmental Engineering, National University of Singapore, Singapore

Correspondence
Yuzhu Li, 1 Engineering Drive 2, E1A, Singapore 117576
Email: pearl.li@nus.edu.sg

ABSTRACT

This work provides a novel approach that combines computational fluid dynamics (CFD) with computational solid mechanics (CSM) to dynamically simulate the fully coupled hydroelastic interaction between nonlinear ocean waves and a submerged-horizontal-plate breakwater (SHPB). Based on a systematic series of simulations, it is shown that the wave damping performance of an SHPB can be evidently improved by an appropriate extent of deformation, which can be achieved through the design of its bending stiffness by varying elasticity and/or aspect ratio. The wave attenuation effect is found to be maximized when an SHPB has a deformation amplitude close to the incident wave amplitude. By accounting for the hydroelastic effect through the fully coupled CFD+CSM approach, this work presents a new computational technique that supports the design of deformable offshore and coastal structures.

1 INTRODUCTION

A submerged-horizontal-plate breakwater (SHPB) is a thin plate that is placed in a certain water depth and spans in the horizontal direction, as shown in Figure 1. The purpose of an SHPB is to attenuate wave attacks on coastal or offshore infrastructures. Compared to other types of wave-control devices, e.g. rubble mound breakwaters, SHPBs require much less material cost and can work in relatively deep waters to avoid being damaged by severe ocean surface waves. Meanwhile, SHPBs have little impact on the marine environment and water circulations (Graw, 1993; Yu, Isobe, & Watanabe, 1995), and the problems causing stability risks that are faced by conventional breakwaters e.g. scour and liquefaction (Sumer & Fredsøe, 2000; Celli, Li, Ong, & Di Risio, 2019) are of minimal concern for SHPBs. Despite these benefits, the performance of SHPBs is very sensitive to the incoming wave condition and its own physical characteristics (Yu, 2002). Therefore, advanced design approaches are required to understand and optimize the performance, before SHPBs can be widely utilized.

Early studies of SHPB were mostly in analytical approaches. The work of Heins (1950) is considered as one of the first studies on a semi-infinite width plate interacting with waves in a finite water depth. The reflection and transmission coefficients were derived using the Wiener-Hopf method. Greene & Heins (1953) then extended the analytical solution to infinite water depth. Burke (1964) further developed a mathematical method for a submerged finite-width plate based on the Wiener-Hopf method. Later, alternative analytical methods such as matched asymptotic expansions (Siew & Hurley, 1977; Patarapanich, 1984) and the eigenfunction expansion method (Ijima, Ozaki, Eguchi, & Kobayashi, 1970; Liu & Iskandarani, 1991; Wang & Shen, 1999) have also been applied to relevant problems. Mohapatra & Shoo (2014) used the eigenfunction expansion method to derive the linear wave interaction with a floating and submerged elastic plate system based on the assumption that the surface water waves and structural response are of small amplitudes.

The analytical solutions mentioned above were only limited to solving linear or weakly nonlinear waves interacting with SHPBs. However, the interaction between propagating waves and an SHPB usually leads to significant nonlinearities (He, Xu, Gao, & Ren, 2018a). In this context, numerical approaches have been applied to study the nonlinear wave-SHPB interaction in recent years. Liu, Huang, & Tan (2009) modelled the transmission of nonlinear waves over the SHPB using a

numerical wave tank and the boundary element method. Qi & Hou (2003) modelled the same problem using the computational fluid dynamics (CFD) method, in which CFD showed a great capability of simulating nonlinear wave behavior over the plate. Jin, Liu, He, & Li (2014) applied a two-phase CFD solver to investigate the performance of a rigid and fixed SHPB in waves, and found that a relatively thin plate has better wave damping performance than a thick one. He, Xu, Gao, & Ren (2018b) and He, Gao, Xu, Ren, & Wang (2019) applied a CFD approach in terms of the smoothed particle hydrodynamics method (a Lagrangian based mesh-free method) to investigate the effect of non-breaking and breaking waves on a fixed SHPB. He, Xu, Gao, & Ren (2018a) and Fu, Zhao, Wang, & Yan (2021) performed numerical simulations of waves interacting with a heaving SHPB; both of the works have found that a heaving plate can be more effective than a fixed one in most of the submerged conditions. Rather than commonly studied horizontal plate, Yueh, Chuang, & Wen (2018) proposed a concept of submerged wavy plate breakwater, which seems to have better wave attenuating performance in certain situations with proper design, but the practicalities such as manufacturing cost and structural strength need to be further investigated. In these CFD studies, although the nonlinear wave effect could be modelled and the flows were simulated with least assumptions (for analytical studies it is common to simplify the flow to Euler flows by neglecting its viscosity), the long thin SHPB plates were all assumed as rigid bodies, because CFD itself does not include structural solutions to account for the SHPB elasticity.

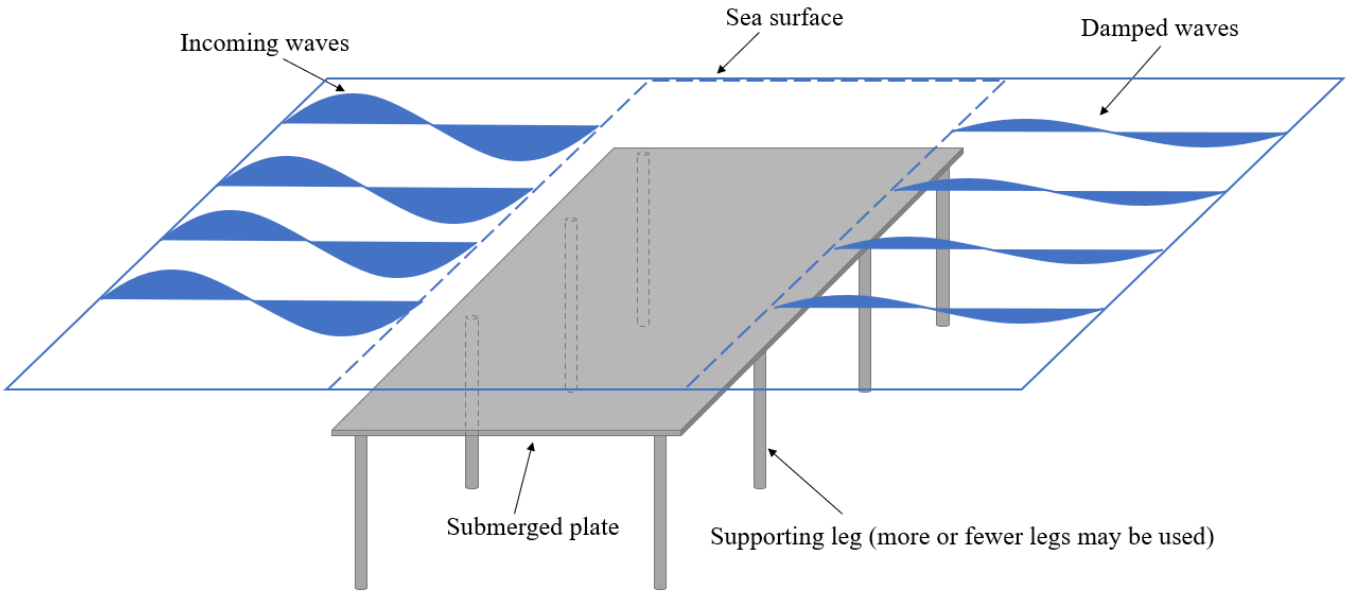

FIGURE 1. Sketch of a submerged-horizontal-plate breakwater; in real life, the device can be approximately 20 m long, 100 m wide and 0.4 m thick (Okubo, Takahashi, Kojima, & Moritaka, 1994; Wang, 2017; He, Gao, Xu, Ren, & Wang, 2019).

In fact, the contemporary rigid-body assumption is not realistic enough for SHPB modelling. As SHPBs are thin plates that are fixed underwater and span in the horizontal direction, their response to waves can be governed by elastic deformations. A deforming SHPB may lead to very different wave damping performance, as the dynamic structural deformation will also change the surrounding flow field. Although the concept of SHPB has been proposed since the 1950s, hydroelastic design of such structures has never been conducted, mainly due to the lack of a computational approach to fully investigate the two-way interaction between the non-linear free-surface waves and the deformable structure.

In this context, the present work intends to incorporate CFD with an additional set of computational structural mechanics (CSM) solutions to account for the wave-induced SHPB deformation and fully simulate the wave-SHPB interaction. Particularly, the present work will couple CFD and CSM via a fully two-way fluid-structure interaction (FSI) algorithm.

In terms of FSI approaches, most contemporary FSI simulations, e.g. McVicar, Lavroff, Davis, & Thomas (2018), Masoomi & Mosavi (2021), adopted a combination of numerical methods/software that uses a finite-volume based tool for fluid solutions (Zhu, Gu, & Chen, 2007) and a finite-element based tool for structural analyses (Park, Kim, & Kim, 2019); this requires an intermediate tool for coupling and data mapping as also pointed out by Huang & Kwon (2020). Therefore, such combined approaches usually increase the computational complexity and the usage of computational memory, and further impose limitations on the mechanism of coupling, which is the principal reason for the simulations to be restricted as one-way coupling, i.e. finite-volume fluid solutions are interpolated into the finite-element model for structural analyses, but the deformed structure does not provide feedback to update the fluid solutions.

Some other works have imported fluid and solid solutions to the same software (although still using different discretizing

methods) and realized a weakly two-way coupling of FSI, e.g. Di Domenico, Groth, Wade, Berg, & Biancolini (2018); Groth, Cella, Costa, & Biancolini (2019). In weakly two-way coupling, per time step the fluid solution is first passed to the solid part to induce the solid deformation and then the solid deformation is used to update fluid mesh; however, the velocity and pressure of the fluid field are not further solved based on the updated fluid mesh. This is only applicable when the solid deformation is very small. If the deformation is large, the weakly coupling approach will induce errors due to inconsistent dynamic and kinematic features between fluid and solid at the interface, as the fluid and solid domains are not sufficiently coupled.

Alongside the one-way coupling and weakly two-way coupling computational approaches, some analytical studies have been able to establish fully coupled solutions, e.g. Coutand & Shkoller (2005), Muha & Canić (2013), and Meylan (2021), but a disadvantage of the analytical approaches is that they are not capable of considering nonlinear wave-structure interactions or accommodating arbitrary polyhedral geometries that are however essential for modern engineering purposes. Overall, as mentioned in Di Domenico, Groth, Wade, Berg, & Biancolini (2018), it is still ongoing work for the field to develop FSI approaches that are capable of modelling engineering problems with high fidelity.

In order to model the present wave-SHPB interaction problem, first, it is essential to model the FSI as two-way coupling, because the interest is to predict the changed wave field in the presence of a deforming SHPB. On top of a two-way mechanism, the coupling procedure needs to go through sufficient iterations to satisfy the dynamic and kinetic conditions, i.e. fully coupling the waves and the deforming structure. Moreover, for the present problem, the waves are required to be modelled as two-phase flows that contain a nonlinear free surface between air and water. The modelling of multi-phase flows is a key gap for most of the available FSI tools, especially the tools that incorporated a fully coupled approach e.g. Richter (2013) who used a fully Eulerian formulation, van Loon, Anderson, van de Vosse, & Sherwin (2007) who used arbitrary Lagrangian-Eulerian formulation, and del Carre, Muñoz-Simón, Goizueta, & Palacios (2019) who used an unsteady vortex lattice method. In these works, the fluid can only be modelled as a single-phase flow, which was mainly designed for aeroelastic problems but not applicable to model offshore wave-structure interactions.

To meet these challenges, the present work introduces a fully coupled hydroelastic CFD+CSM approach to simulate the FSI between waves and an SHPB. The present approach is developed in OpenFOAM which is an open-source C++ framework for the development of CFD-based solvers (the implementation is described in detail in the report of Huang (2018)), and is built upon the initial finite-volume FSI framework of Tukovic, Cardiff, Karac, Jasak, & Ivankovic (2014). To the best of the authors' knowledge, the present approach is the first integrated model that is able to fully couple ocean waves with deformable structures in the finite-volume based framework, and it has initially revealed promising capabilities in modelling floating sea ice in ocean waves (Huang, Ren, Li, Tukovic, Cardiff, & Thomas, 2019). It is worthwhile to mention that, in Huang, Ren, Li, Tukovic, Cardiff, & Thomas (2019), the sea ice is semi-rigid and freely floating, thus the wave-induced deformation and hydroelastic behavior was inconspicuous. Therefore, the present study for the first time adopts such a CFD+CSM approach to tackle a hydroelastic interaction containing large nonlinear deformations, which can occur to the side-mounted SHPBs in waves. An utmost computational challenge of the present work is to couple large nonlinear deformations of structures with free-surface wave motions and iterate the solutions until achieving a fully coupled and accurate manner. The applied CFD and CSM equations are solved through discretization and the solutions are second-order accurate in both space and time, where the numerical interpolation uses the solution at the current grid/time and those from the adjoint two cells/previous two time levels, instead of from only one adjoint cell/previous time level. The present approach is also capable of accommodating arbitrary polyhedral meshes, which makes it applicable to modern industrial applications. In addition, the meshes of fluid part and solid part are geared in the same computational domain rather than connected through a multiplier (van Loon, Anderson, van de Vosse, & Sherwin, 2007), which replicates the case with high fidelity and can avoid the multiplier to bring about uncertainty.

The present paper starts by demonstrating the CFD+CSM approach to build a computational model for the hydroelastic interaction between ocean waves and offshore/coastal structures. Based on the unique capability of the new model, it is applied to simulate a deformable SHPB in the process of wave attenuation, and a series of verification studies (grid convergence studies) and validation against existing experiments are presented. Then, by varying the elasticity and aspect ratio of an SHPB and comparing the waves downstream, the role of SHPB deformation in the process of wave attenuation is derived. In particular, an innovative design strategy is provided on utilizing the SHPB deformation to maximize its wave damping performance.

2 COMPUTATIONAL APPROACH

The present CFD+CSM simulation approach solves both fluid and structural domains, alongside an FSI algorithm to stitch the solutions together. In order to fulfil this, the whole simulated domain is split into two sub-regions, i.e. the fluid sub-region (including air and water) and the solid sub-region (the SHPB structure). These two sub-regions are connected via the interface in between. The fluid sub-region simulates a desirable wave field and predicts the wave evolution, whilst the solid sub-region represents a thin elastic SHPB placed at a vertical distance to the water surface and solves its deformation. The computational practicalities are explicated as follows.

2.1 Computational domain

A rectangular fluid domain is established in a two-dimensional Cartesian *x*-*y* coordinate system, as shown in Figure 2. The computational domain is assumed as two-dimensional (i.e. uniform in the spanwise direction) based on the condition that the device is side-mounted and spans extensively in the profile direction to cover the protected coastline, and the considered incoming waves are only propagating along the landwards direction. This two-dimensional assumption has also been used in contemporary SHPB studies, e.g. Jin, Liu, He, & Li (2014), Yueh, Chuang, & Wen (2018), He, Gao, Xu, Ren, & Wang (2019), Fu, Zhao, Wang, & Yan (2021). It is deemed to have a negligible influence on the results of the present study, as will also be validated in Section 3 against three-dimensional experiments. Such a simplification in dimension can significantly save the computational cost thus allowing a large number of simulation cases to be performed and thereby sufficiently study the influential parameters.

In Figure 2, the *x*-axis denotes the horizontal direction whilst the *y*-axis denotes the vertical direction. The domain size is 12 m in length and 0.4 m in height. It contains water to a depth of *D* and above which is air. The top and bottom boundaries of the domain are defined as a static pressure condition and a no-slip wall to model the atmosphere and the seabed, respectively. The left and right boundaries of the domain are set as wave inlet and outlet, in which regular waves propagate towards the *x*-positive direction. The incoming waves are simulated using the second-order Stokes theory as implemented in the "waves2Foam" toolbox (Jacobsen, Fuhrman, & Fredsøe, 2012) developed in the OpenFOAM framework. This toolbox has been successfully applied to simulate waves for multi-physics problems such as the wave-structure-seabed interaction (Li, Ong, & Tang, 2018; 2020).

An elastic plate is placed underneath the free surface, which represents an SPHB, as shown in Figure 2. The vertical distance from the plate to the undisturbed water surface is denoted as *d*; the length and thickness of the SHPB are denoted as *L* and *h*, respectively. The SHPB plate has its left and right boundaries clamped while its top and bottom boundaries are fully flexible. The clamped condition at two edges is considered since strong support is needed to keep the breakwater plate in place even in rogue waves. Meanwhile, it is assumed that the spacing between supporting legs is not large enough to allow a notable deformation between two legs in the spanwise direction (as shown in Figure 1). At upstream and downstream of the plate, two wave gauges are positioned to record the free surface variance in the time domain.

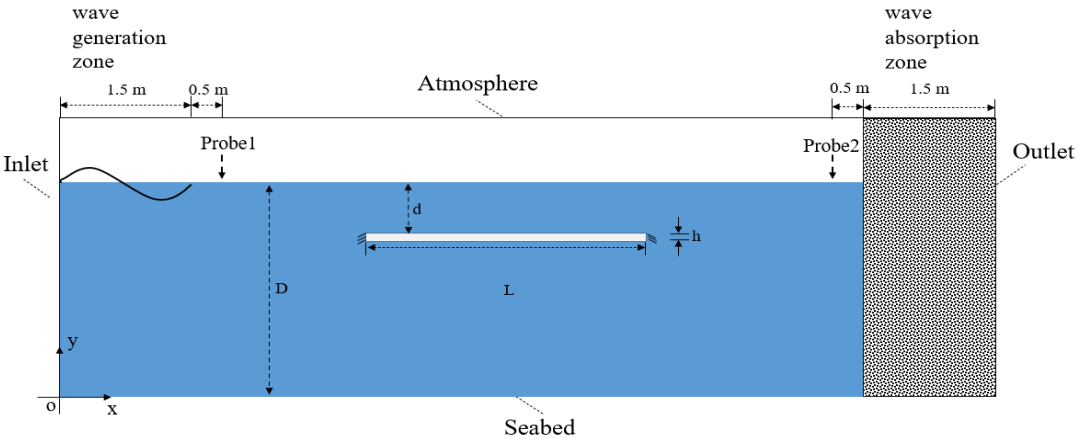

FIGURE 2: The computational model: in a numerical wave tank, a submerged horizontal plate is placed, whose upper and lower boundaries are deformable, while left and right boundaries are clamped. The domain is designed in a model scale to allow validation against experiments, whilst the scale factor is approximately 1:30 to real life.

2.2 Computational method

In the present computational process, the fluid (air and water) and solid (SHPB) sub-regions are discretized into non-overlapping cells using the finite volume method, allowing the calculation of corresponding fluid and structural solutions in the spatial domain. The discretized fluid mesh and solid mesh are shown in Figure 3. The optimal mesh densities for both the sub-regions are investigated through convergence studies, to be presented in Section 3. The fluid mesh is built to obtain CFD solutions, e.g. pressure/velocity fields and the location of free surface, through solving the Navier-Stokes equations together with the volume of fluid (VOF) method. The solid mesh is built to obtain CSM solutions, i.e. SHPB deformation. The deformation solution is fully nonlinear, solved based upon the conservation of momentum which applies the St. Venant Kirchhoff hyperelastic method to express the stress. The mathematical formulae of the CFD and CSM equations are given in Appendices A and B.

It is noted that this study does not include a turbulence model since no turbulent phenomenon is expected to occur for the present simulated conditions. For the main computational wave condition, the Reynolds number is approximate 6×10^4, using the maximum orbital velocity at the plate depth ($v' \approx 0.1$ m/s assumed from the Stokes wave theory), which is far below the critical Reynolds number where the flow becomes turbulent on a plate ($\approx 5 \times 10^5$). Also, the Keulegan-Carpenter

number ($KC = v' T_w/L$) is relatively small with a value of 0.2 for such wave condition, where v' is the again the maximum orbital velocity at the plate depth and T_w is the wave period. A value of KC smaller than 1 indicates that the flow does not separate from the plate (Sumer & Fredsøe, 2006), thus no turbulence effect is considered in the present study.

To acquire the transient status for both fluid and solid sub-regions over a sufficient time duration, the total solution time is discretized into certain segments of time steps. The size of each time step is ascertained by the Courant number ($Co = v\Delta t/\Delta x$), where Δt denotes the time step size, v is the flux speed through the shared face between two neighboring cells, and Δx is its distance between the centers of these two cells. There exists a maximal value of $v/\Delta x$ in the whole domain for each time step, with which the time step size is automatically determined following the constraint of $Co \leq 1$. Comparing to setting a fixed time step size, this self-optimizing algorithm for the time step size significantly improves the computational efficiency.

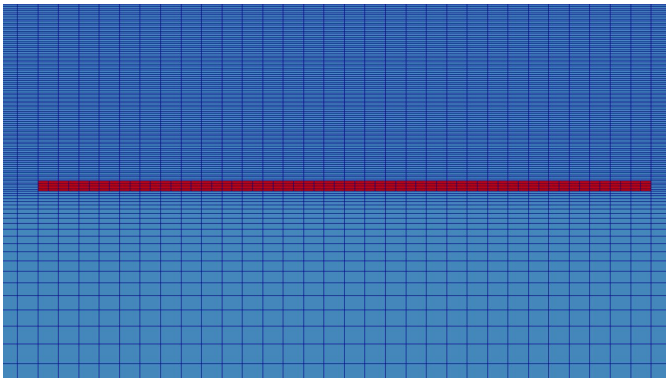

(a) Combined fluid and solid mesh

(c) Zoom-in solid mesh around the left edge of the plate

FIGURE 3. Mesh layout of the model with blue denoting fluid mesh and red denoting solid mesh. Green lines indicate the interface boundaries at both the fluid and solid sub-regions. The fluid domain above the plate contains the free surface between water and air, thus the fluid mesh above the plate is set to be denser than the fluid mesh below the plate.

The CFD and CSM solutions are coupled via a partitioned scheme proposed by Tukovic, Karac, Cardiff, Jasak, & Ivankovic (2018), where the fluid and solid solutions are obtained by turns, and the kinematic and dynamic conditions are matched at the fluid-solid interface. The kinematic condition states that the velocity and displacement are continuous across the interface as expressed in Equations (1) and (2); the dynamic condition states that forces are in equilibrium at the interface as expressed in Equation (3).

$$\boldsymbol{v}_{fluid} = \boldsymbol{v}_{solid} \quad (1)$$

$$\boldsymbol{u}_{fluid} = \boldsymbol{u}_{solid} \quad (2)$$

$$\boldsymbol{n} \cdot \boldsymbol{\sigma}_{fluid} = \boldsymbol{n} \cdot \boldsymbol{\sigma}_{solid} \quad (3)$$

where $\boldsymbol{v}$ is the velocity vector, $\boldsymbol{u}$ is the displacement vector, $\boldsymbol{n}$ is the normal vector at the interface, and $\boldsymbol{\sigma}$ is the stress tensor.

A two-way fully coupling procedure is achieved in this work. First, the pressure and velocity fields are solved in the fluid sub-region through CFD, giving the fluid force on the interface. The fluid force field on the interface provides a boundary force for the solid sub-region, where Equation (3) is satisfied. Then, the deformation of the solid body is solved through CSM. The deformation induces displacements of all the solid cells, and the derivative of the displacement field of the interface gives a velocity field, which is passed back to the fluid sub-region, where Equation (1) is satisfied. For each time step, iterations are performed until Equation (2) is satisfied. The iteration procedure is illustrated in Figure 4 and described as follows:

1) At the beginning of every time step, the displacement of the solid sub-region is updated using the results of the previous time step. Then, the Aitken coupling scheme is employed for improving the convergence speed during the coupling procedure, which uses an Aitken Relaxation Factor (*ARF*) to minimize the numerical residual:

$$ARF_{i+1} = ARF_i \times \left[1 - \frac{\sum(Res_i \cdot \Delta Res_i)}{\sum(\Delta Res_i \cdot \Delta Res_i)}\right] \quad (4)$$

where i is the ith iteration. The residual (*Res*) is calculated by the solid interface displacement minus the fluid interface displacement (*SID* – *FID*). Following Equation (4), *ARF* is updated according to *Res*. Then the fluid mesh is updated based on the new *ARF* value:

$$\text{Fluid Mesh}_{i+1} = \text{Fluid Mesh}_i + ARF_{i+1} \times Res_i \quad (5)$$

Then the derivative of *FID* is computed to obtain the velocity of the fluid interface, and this interface velocity induces the mesh motion for the fluid domain.

2) Using the updated mesh, the new velocity and pressure fields within the fluid sub-region are calculated using the fluid solver.

3) The velocity and pressure results are used to calculate the fluid force at the interface, and then the force field on the interface is transferred from the fluid sub-region to the solid sub-region.

4) Having the fluid force on the interface, the induced solid deformation is calculated by the structural solver, recorded as the displacement of all cells in the solid sub-region.

5) *SID* is then obtained from the boundary cells' displacements and then compared with *FID* to update *Res*. The

solver enters the next timestep when *Res* is smaller than the prescribed residual criterion.

In this work, the criterion for *Res* is restricted to be smaller than 1×10^{-6} m, which is achieved by averagely 20 FSI iterations per time step. Verification of the proposed procedure has been conducted against a commonly used FSI benchmark case, as presented in Appendix C.

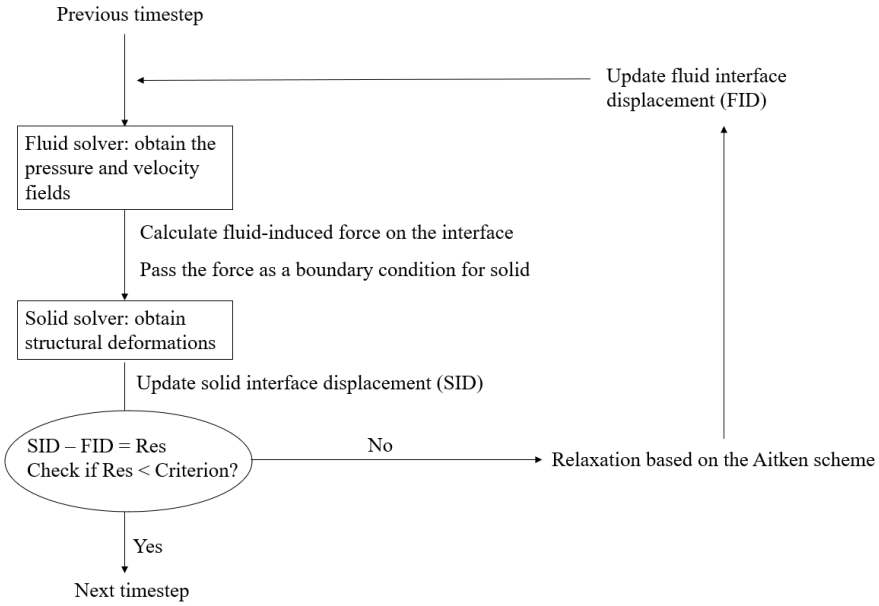

FIGURE 4. Solution procedure of the FSI inner loop.

3 VALIDATION AND VERIFICATION

3.1 Grid convergence study for wave modelling

The accuracy and computational cost of wave modelling are affected by the fluid mesh density. Sensitivity tests were performed to find out the optimal grid numbers, for which various cell numbers per wave height (M) were used with M = 5 - 15. Meanwhile, 100 cells per wavelength were held, which is the minimal cell number matching with M = 5 - 15 to secure an error of less than 1% (Connell & Cashman, 2016). The corresponding free surface elevations were recorded using the probe downstream as illustrated in Figure 2. It is shown in Figure 5 that, with M > 10, the targeted wave field can be obtained and stably propagate downstream. Since there is no obvious difference between the results from M = 10 and M = 15, M = 10 is chosen as the vertical fluid mesh density in the free surface region, which can minimize the computational cost and meanwhile maintain the computational accuracy.

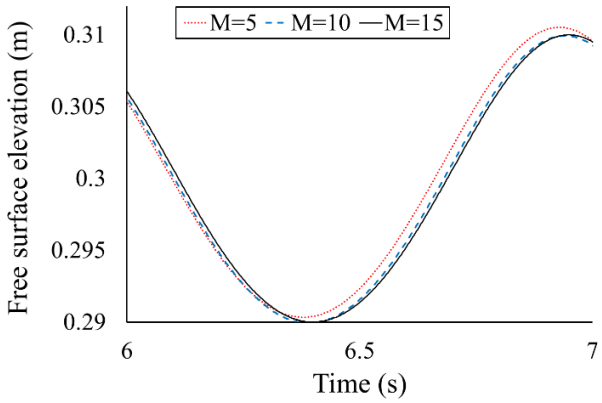

FIGURE 5. Downstream free surface elevation obtained using various cell numbers per wave height. The simulated wave condition is with T_w = 1.1 s and H = 0.02 m.

3.2 Validation of deformation solution

There is a lack of experimental data for detailed measurement of the deformation of a submerged plate. However, Sree, Law, & Shen (2017) reported the measurement for the wave-induced deformations of a similar plate placed at the water surface. Therefore, the experiment of Sree, Law, & Shen (2017) was reproduced to validate the accuracy of the present computational approach in modelling the plate deformation in waves. Four sets of solid mesh were used to ascertain a suitable density to discretize the thin plate, consisting of 200 - 800 cells. Wave-induced deformations in terms of the non-dimensional vibration amplitudes (plate vibration amplitude a divided by its thickness h) were measured over the plate, as presented in

Figure 6. The experimental condition is T_w = 0.7 s and H = 0.017 m. The plate is 1 m long and 0.01 m thick, and the rheological properties of the plate are with density ρ = 910 kg/m^3, Young's modulus E = 870 MPa and Poisson's ratio υ = 0.3.

It can be seen in Figure 6 that the model prediction with the four sets of mesh generally agrees with the measurements. The discrepancy between computational and experimental is minimal and does not notably change as long as the solid cells are more than 400. Thus a grid number of 400 were employed to discretize the solid sub-region for further simulations, which consists of 100 cells in the plate length direction times four cells per plate thickness.

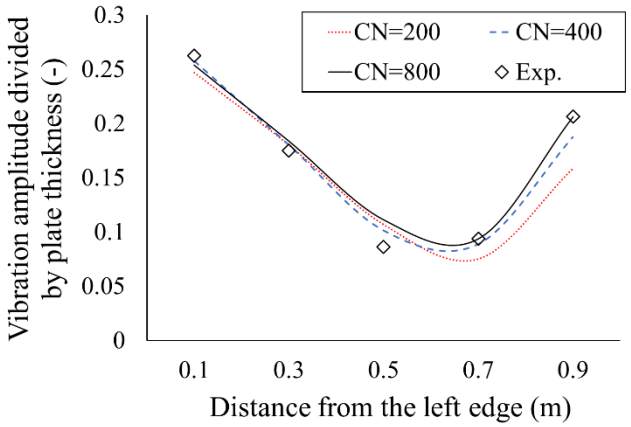

FIGURE 6. Plate deformation obtained with varying cell numbers (CN) for the solid mesh, comparing with the measurements of Sree, Law, & Shen (2017). The plate length is 1 m in total and the x-axis shows the measured distance from its left edge.

3.3 Validation of wave interactions with an SHPB

The simulation of wave reflection and transmission in the presence of an SHPB was validated against the experiments of Liu, Huang, & Tan (2009). The SHPB investigated in their experiments was 0.6 m long and 0.01 m thick, made by a Perspex material (polymethyl methacrylate) with ρ_{solid} = 1180 kg/m^3, E = 2.3 GPa and υ = 0.316. The selected experimental conditions are D = 0.3 m, d = 0.1 m, H = 0.02 m and a range of incident wave periods T_w = 0.8 - 1.5 s. The reason for these selections was that these conditions were reported by Liu, Huang, & Tan (2009) to present drastic wave-SHPB interactions, and the most conspicuous wave attenuation was produced within this range.

$$R = \frac{|a_{\text{upstream}} - a_{\text{incident}}|}{a_{\text{incident}}} \quad (6)$$

$$T = \frac{a_{\text{downstream}}}{a_{\text{incident}}} \quad (7)$$

The validation of the wave-SHPB interaction is shown in Figure 7, presenting good accuracy for all the tested wave range, and the maximal wave damping point appears at the same wave period as that in Liu, Huang, & Tan (2009).

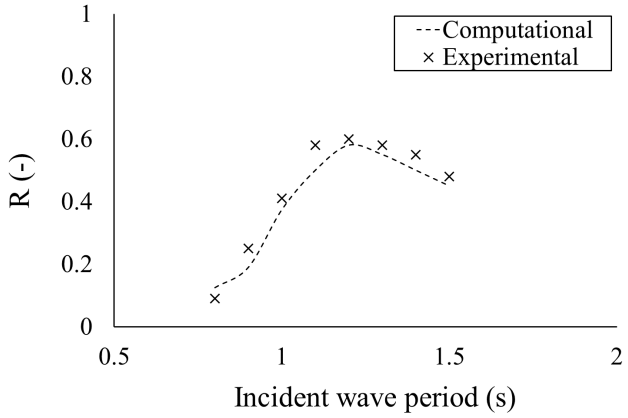

(a) Reflection coefficient

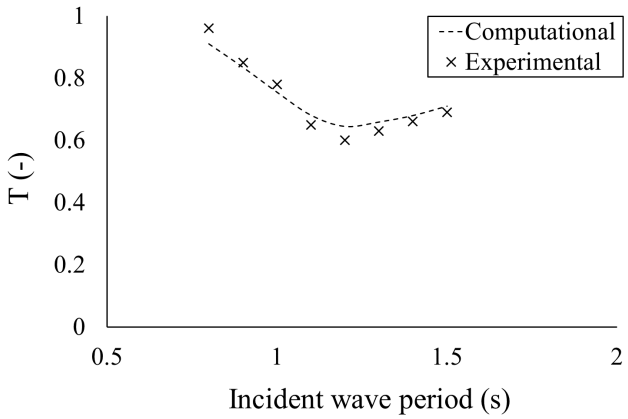

(b) Transmission coefficients

4 HYDROELASTIC ANALYSES AND DESIGN OPTIMIZATION

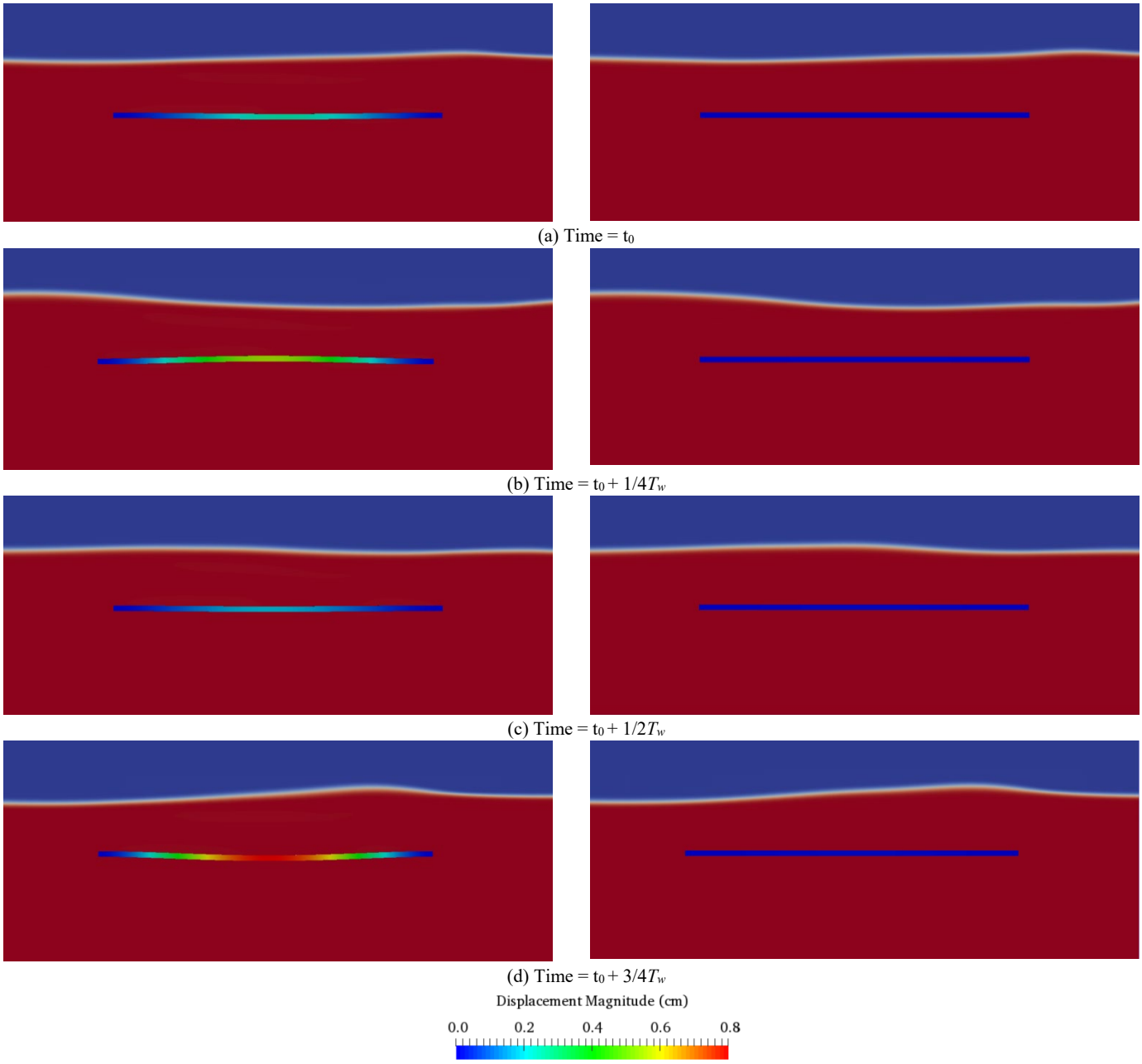

FIGURE 8. Comparison of wave-SHPB interaction between the flexible (left) and stiff (right) materials. The applied wave condition in this figure is T_w = 1.1 s and H = 0.02 m. In the subfigures, in red beneath the free surface is the water phase while in blue above the free surface is the air phase.

4.1 The hydroelastic effect

To analyze the influence of SHPB deformation on its wave damping performance, simulations were conducted with two SHPBs respectively with flexible and stiff materials. The selected flexible material is a common rubber type with E = 50 MPa, and the stiff one is a Perspex material whose E = 2.3 GPa. Both materials have $\rho_{solid} = 1180\ \mathrm{kg/m^3}$ and $\nu = 0.316$ (Engineering Toolbox, 2003). The SHPB geometry is kept at 0.6 m long and 0.01 m thick to be in line with the validation study.

As shown in Figure 8, whilst the rubber material (left-hand side) presents notable deformations following the wave motion, the Perspex material (right-hand side) presents a semi-rigid behavior under the wave impact. The flexible plate bends upward/downward when a wave trough/crest arrives upon it. The maximal displacement amplitude occurs around the middle point of the plate. Figure 8(d) shows that the maximal displacement occurs when the flexible plate bends downward; the magnitude is around 0.75 cm, ≈75% of the plate thickness or the incident wave amplitude.

The wave damping performance of these two materials was found to be significantly different, in which the flexible material reveals to be much better. Figure 9 compares the time-series free surface elevation measured downstream, which shows a notably reduced wave motion by applying the flexible material. This indicates that a notable plate deformation may significantly enhance the wave damping performance. Figure

10 decomposes the downstream waves in different frequencies by FFT, which shows the reduced wave amplitude mainly attributes at its fundamental frequency, i.e. the incident wave frequency.

The influence of SHPB deformation on wave transmission has been further investigated over a range of incident wave periods, as shown in Figure 11. It shows that a flexible plate can have a better wave attenuation effect than a very stiff one for all the examined wave periods. The hydroelastic effect is conspicuous as the wave transmission coefficient is reduced by approximately half. This difference is of great importance because wave damping is the utmost purpose of such breakwater structures. With the present CFD+CSM approach accounting for the SHPB deformation in the interaction process, it becomes feasible to investigate the influence of SHPB's deformation on its wave damping performance, which is expected to be an important advancement for the SHPB design.

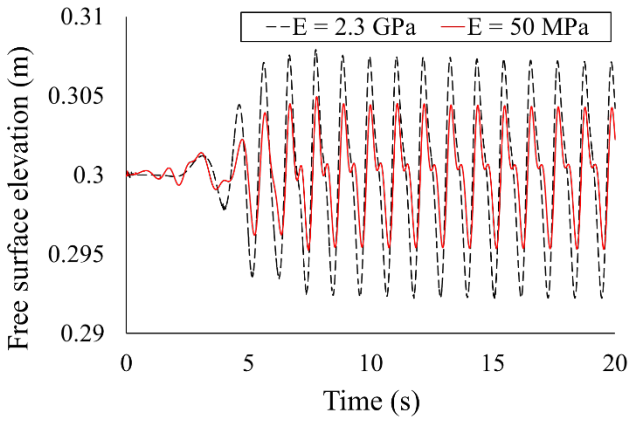

FIGURE 9. Comparison of downstream free surface elevation between the flexible and stiff materials. The applied wave condition in this figure is T_w = 1.1 s and H = 0.02 m.

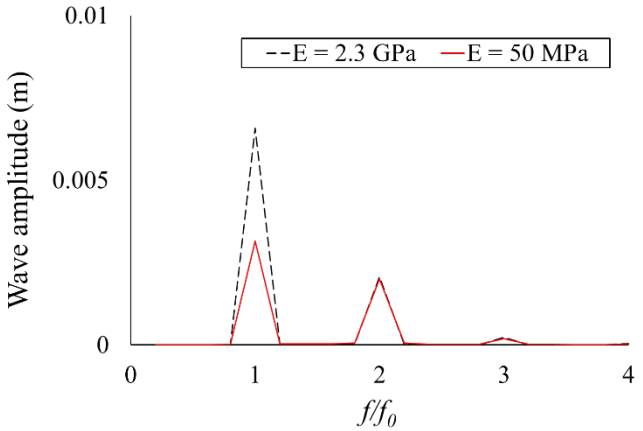

FIGURE 10. Comparison of downstream wave amplitude at different frequencies, between the flexible and stiff materials. f/f_0 denotes the breakdown frequencies of downstream waves normalized by the incident wave frequency i.e. $f_0 = 1/T_w$. The applied wave condition in this figure is T_w = 1.1 s and H = 0.02 m.

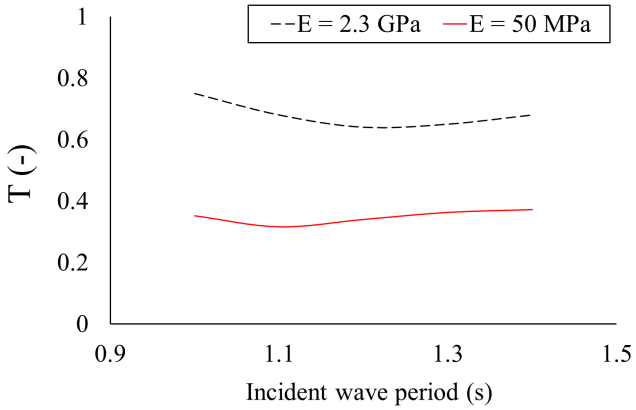

FIGURE 11. Comparison of the transmission coefficient between flexible and stiff materials.

4.2 The influence of elasticity

Following the finding that the SHPB deformation can significantly influence the associated wave attenuation, the next step is to investigate how to design the hydroelastic response of an SHPB so as to optimize its wave damping performance. To achieve this purpose, simulations were performed with subtle variations of Young's modulus that are close to the rubber material.

The SHPB deformation is shown as periodic vibrations following the incident waves. Figures 12 and 13 present the maximum deformations (upward and downward) of the plates with different E applied. In these two figures, it can be seen that changing Young's modulus by 5 MPa can induce a pronounced difference in the SHPB vibration magnitude, which may further induce an influential change in the downstream wave field. Hence, it is essential to investigate the sensitivity of the downstream wave to the elasticity of an SHPB.

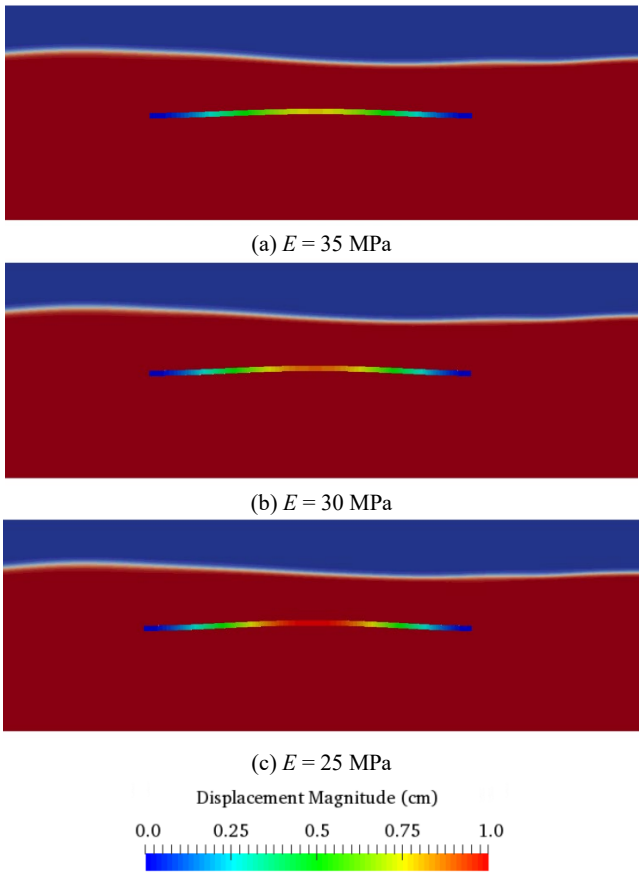

FIGURE 12. Snapshots when the SHPB reaches its upward deformation limit, for varying elasticity.

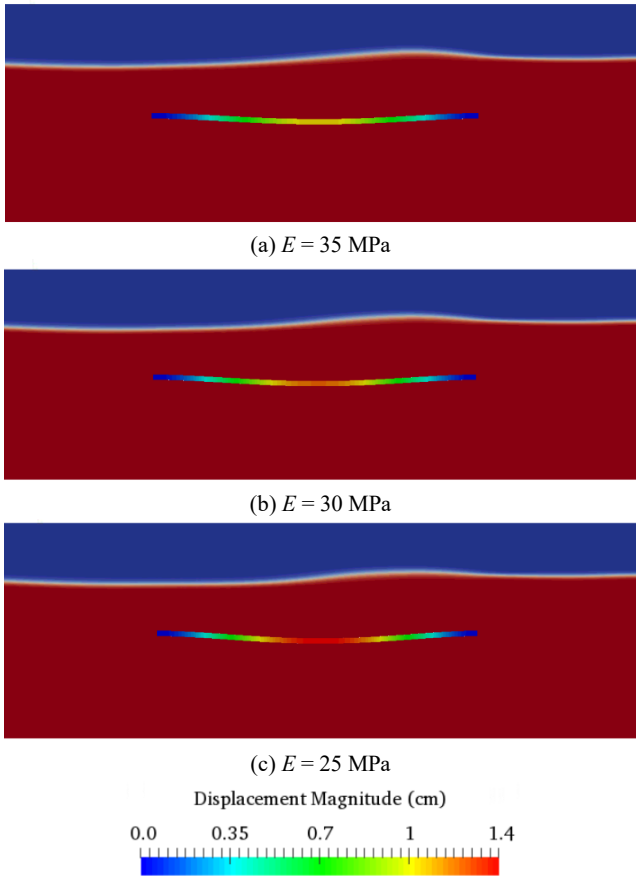

FIGURE 13. Snapshots when the SHPB reaches its downward deformation limit, for varying elasticity.

To analyze in detail the influence of SHPB deformation on the wave attenuation, Figure 14 shows the FFT breakdown of the downstream wave profiles with several selected E values for the SHPB. It shows that the wave amplitude at the fundamental frequency reaches a negligible level when E = 30 MPa; the downstream wave amplitude at the fundamental frequency is larger when either a larger or lower E was applied. This suggests the existence of an optimal E for a specific SHPB design task. Meanwhile, the wave amplitude at the secondary frequency decreases with a smaller Young's modulus in the whole examined range. This indicates that a larger deformation can better break the secondary wave profile, but this is inapplicable to the fundamental wave profile.

As the design purpose of SHPB is to minimize the total wave energy that can transmit downstream (W_{ds}), the downstream wave energy was integrated over the frequency domain, as expressed in Equation (8).

$$W_{ds} = \frac{1}{2}\int_0^{\infty} \hat{a}^2 \, df \tag{8}$$

where $\hat{a}$ is the wave amplitude at the specific frequency.

In this context, optimizing the SHPB performance essentially means minimizing W_{ds}. For this purpose, the relation between W_{ds} and the deformation amplitude of the SHPB is established. The deformation amplitude of an SHPB (a_{SHPB}) is calculated as the average of its upward and downward deformation limits, and the correlation between a_{SHPB} and W_{ds} is shown in Figure 15. Table 1 provides the tested conditions and results in detail. Figure 15 reveals a nonlinear relationship between a_{SHPB} and W_{ds}, i.e., W_{ds} decreases with the SHPB deformation getting stronger, reaches the minimum when $a_{SHPB}/a_{incident} \approx 1$, and then starts to increase again. This signifies a potential optimal strategy to minimize the transmissible wave energy over an SHPB.

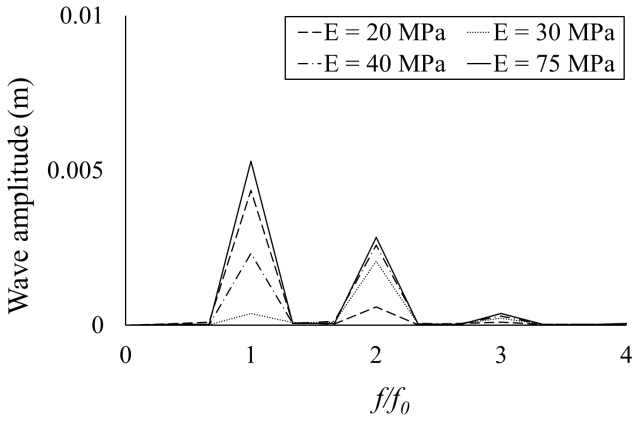

FIGURE 14. Comparison of downstream wave amplitudes at different frequencies, with a range of E applied to the SHPB. The applied wave condition in this figure is T_w = 1.1 s and H = 0.02 m.

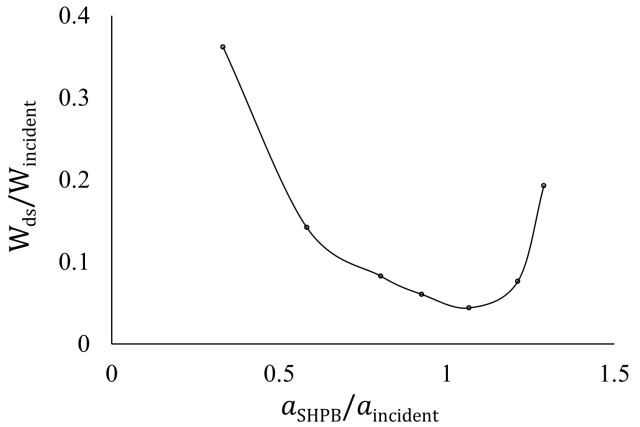

FIGURE 15. Downstream wave energy normalized by incident wave energy ($W_{ds}/W_{incident}$) as a function of deformation amplitude of the SHPB normalized by the incident wave amplitude ($a_{SPHB}/a_{incident}$), which changes due to varying E of the SHPB. The applied wave condition in this figure is T_w = 1.1 s and H = 0.02 m.

TABLE 1. Downstream wave energy obtained with different Young's moduli applied to the SHPB. The applied wave condition is T_w = 1.1 s and H = 0.02 m.

Young's modulus of the SHPB	SHPB deformation upward limit	SHPB deformation downward limit	Amplitude of the deformation	Downstream wave energy over incident wave energy
E (MPa)	a_{up}(cm)	a_{down} (cm)	$a_{SHPB} = \frac{1}{2}(a_{up} + a_{down})$ (cm)	$W_{\mathrm{ds}}/W_{\mathrm{incident}}$
20	1.10	1.48	1.29	0.190
25	1.03	1.40	1.21	0.076
30	0.90	1.23	1.07	0.044
35	0.77	1.08	0.92	0.060
40	0.65	0.96	0.80	0.082
50	0.41	0.75	0.58	0.141
75	0.19	0.47	0.33	0.361

4.3 The influence of aspect ratio

To further analyze the FSI effect and derive a generic optimal strategy for SHPB design, the aspect ratio (AR = L/h) of the SHPB has been varied to investigate the effect on the wave damping. Using a rubber SHPB as the basis, and the AR was varied in a range of 40 to 120, from a relatively thick plate that occurs minimal wave-induced deformation, to a relatively thin plate that bends dramatically with the wave motion, as shown in Figure 16. It is obvious that the larger AR, the larger vibration amplitude for the plate (noting that a larger vibration amplitude does not necessarily lead to a greater wave damping performance). In each sub-figure of Figure 16, the downward amplitude is generally larger than the upward amplitude, which is because of the nonlinear wave effect; this also demonstrates again that the present CFD and CSM solutions are nonlinear. Table 2 further calculates the amplitude of plate deformation and the downstream wave energy for all tested ARs.

Figure 17 plots the relation between the nondimensional a_{SHPB} and W_{ds} whilst varying AR. It can be seen that the trend agrees very well with that in Figure 15. This confirms that the essential reason for the changed wave damping performance is the SHPB's vibration amplitude, which can result from changing either E or AR or both, i.e. its bending stiffness. The optimal condition is unified: when the vibration amplitude is close to the incident wave amplitude, the downstream wave energy is minimized to a level of less than 10% of the incident wave energy. Thus, it is a very important and beneficial step to perform the hydroelastic design so that an SHPB can damp waves to such a level, as the FSI effect appears to be sensitive and neglectful design could easily allow more than 40% wave energy to pass.

Combining the influences of E and AR further indicates the underlying mechanism between the hydroelastic FSI and the wave damping performance: the plate deformation can act as an obstacle for the wave flow, and the obstacle is most effective when the plate bends to the same extent as the wave heaves, showing a resonant behavior that eliminates most of the incident wave. The plate can be too stiff to show the FSI effect, or too flexible that performs a compliant behavior to the waves; in either of the situations, a large portion of the wave energy can still pass, which results in an unideal wave damping performance.

The above results demonstrate a strategy to perform hydroelastic SHPB design, by selecting appropriate E and AR so that the breakwater device can undertake a desirable deformation to minimize the downstream waves. In the design circles, it is recommended to analyze the deformation of SHPB in the primary wave condition that it is expected to operate at, with a target of $a_{SHPB}/a_{incident} \approx 1$. The present CFD+CSM approach provides a practical and robust tool to perform the design task. In particular, this approach overcomes the limitation of previous computational works that only can assume SHPBs as rigid, and this advancement has shown to be significant.

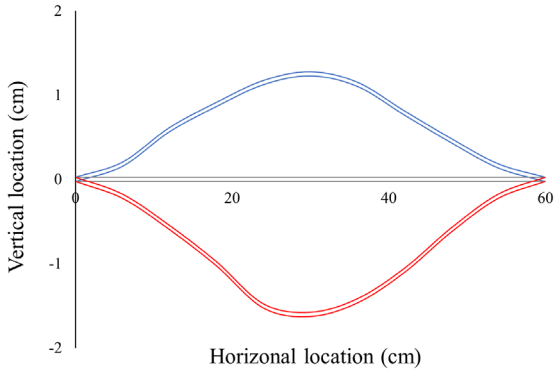

(a) AR = 120

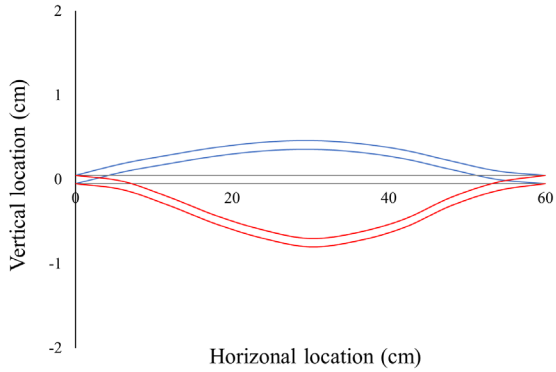

(b) AR = 60

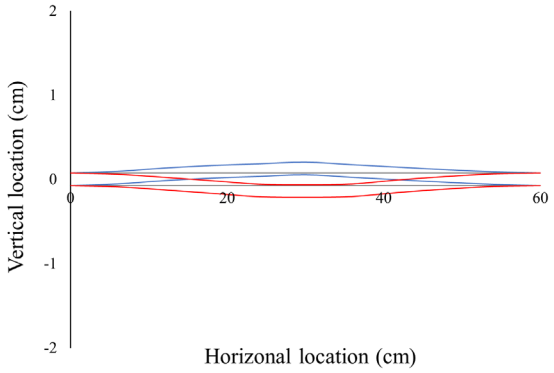

(c) AR = 40

FIGURE 16. Upward and downward limits of the wave-induced SHPB deformation, obtained with plates of different aspect ratios. The applied wave condition in this figure is T_w = 1.1 s and H = 0.02 m.

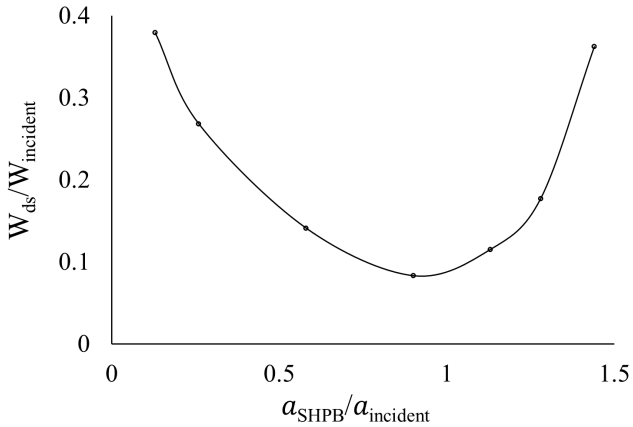

FIGURE 17. Downstream wave energy normalized by incident wave energy ($W_{ds}/W_{incident}$) as a function of deformation amplitude of the SHPB normalized by the incident wave amplitude ($a_{SHPB}/a_{incident}$), which changes due to varying AR of the SHPB. The applied wave condition in this figure is T_w = 1.1 s and H = 0.02 m.

TABLE 2. Downstream wave energy obtained with different aspect ratios applied to the SHPB. The applied wave condition is T_w = 1.1 s and H = 0.02 m.

Aspect ratio of the SHPB	SHPB deformation upward limit	SHPB deformation downward limit	Amplitude of the deformation	Downstream wave energy over incident wave energy
AR (-)	a_{up}(cm)	a_{down} (cm)	$a_{SHPB} = \frac{1}{2}(a_{up} + a_{down})$ (cm)	$W_{ds}/W_{incident}$
120	1.25	1.62	1.44	0.362
100	1.10	1.36	1.28	0.177
90	0.97	1.29	1.13	0.115
80	0.75	1.04	0.90	0.083
60	0.41	0.75	0.58	0.141
48	0.24	0.28	0.26	0.268
40	0.13	0.13	0.13	0.379

5 DISCUSSION

This section discusses the applicability of the presented computational approach in the practical engineering of SHPB, including potential limitations, the corresponding solutions, and future works.

1) **The scale of the present simulations.** The present study is conducted in a model scale for the purpose of validation against available experiments. In principle, the present CFD+CSM approach can likewise be applied to full-scale investigations. One advantage of CFD studies is the ability to overcome the scale restriction of laboratory studies. Provided the verification and validation in this work, it is feasible to use the present model to directly conduct simulations in the real scale of a design task. This is easily achievable by enlarging the domain and the structure, adjusting mesh sizes, and applying wave conditions of the target geographical location. Regarding the findings, this work demonstrates that the wave damping performance can be maximized when an SHPB is deformed at the same amplitude as the incident wave. This finding can be extended to the full scale (such that the wavelength and SHPB length are tens of meters) based on the Froude similarity, i.e. Froude number ($Fr = v/\sqrt{gL}$) is the same for model and full scales, where g is the gravitational acceleration. Although the disparity of Reynolds number between the two scales could alter the findings, the present investigated wave-structure interactions are mainly due to gravity/inertia forces, and the Reynolds (viscous) effect is fairly small in this case. Therefore, the derived optimal condition is expected to be applicable to full-scale SHPBs.

2) **Other influential factors.** In addition to the present analyzed factors in terms of the elasticity and aspect ratio, the wave-structure interaction could also be affected by other factors such as water depth, since the seabed can have a considerable effect on the wave motion. This is not a concern for the CFD+CSM model, as it can automatically incorporate the seabed boundary according to the design condition, and the principle of designing the SHPB to have a similar vibration amplitude as the dominant wave should be the same. For the effect of plate length, since it has been examined in many previous studies using a rigid-plate assumption, e.g. Liu, Huang, & Tan (2009), He, Gao, Xu, Ren, & Wang (2019), it is not repeated in the present work which focuses on obtaining novel insights into the hydroelastic interaction. The conclusion regarding the influence of plate length is that the wave damping is most effective when the SHPB's length is approximately half of the wavelength. Depending on the specific scenario, material damping may also affect the results if it is significant. In the present case, material damping may be negligible because the continuous and periodic incitation from waves makes the damping over time inconspicuous, which can be corroborated by e.g. the validation of Meylan, Bennetts, Cavaliere, Alberello, & Toffoli (2015), where the experimental-theoretical comparison shows that an elastic model without material damping can well replicate a thin plate's deformation in continuous waves. However, material damping may be significant when investigating the vibration of a structure due to a short and strong impact, where the vibration decays over time e.g. under seismic loads. In that case, material damping can be considered in the present computational model by adding a damping term in the structural governing equations, as the proposed open-source model has full flexibility to also consider additional material properties.

3) **Realistic ocean wave conditions.** In the realistic ocean environment, incoming waves can be a series of wave trains that are constitutive of different wavelengths and heights, thus it is recommended to apply a representative wave condition for the target geographical location and use the present CFD+CSM approach to evaluate the SHPB design accordingly. As a more advanced solution, it is possible to dynamically control the SHPB vibration to optimize the performance in varying sea conditions. Real-time control of such large and flexible structures can be potentially achieved with effective methodologies such as the wavelet-hybrid feedback-least mean square algorithm (e.g. Adeli & Kim, 2004; Kim & Adeli, 2005) or machine learning algorithms (e.g. Anderlini, 2018). Once the SHPB is installed in a real ocean environment, continuous monitoring of such a large-scale structure is of high importance to optimize the performance, reduce structural risks, and improve maintenance and repair strategies. Wavelet transform is a powerful tool to deal with complex signals from the sea, which can consist of dynamic disturbances due to waves, winds, marine structures, and other noisy environmental signals. Methodologies based on the wavelet transform have been proposed for monitoring the condition of large structures (e.g. Zhou & Adeli, 2003; Amezquita-Sanchez & Adeli, 2015a, 2015b; Perez-Ramirez, Amezquita-Sanchez, Adeli, Valtierra-Rodriguez, Camarena-Martinez, & Romero-Troncoso, 2016; Amezquita-Sanchez, Park, & Adeli, 2017).

4) **Future works.** The present model has been applied to the case study of an elastic SHPB. The design has mainly focused on optimizing the wave attenuation performance of the elastic SHPB body, whilst the supporting legs are assumed as fixed boundary conditions at two sides. Further component designs such as the structural analysis of the supporting legs under wave loads should be performed since the design of the support legs is crucial to avoid the risks of structural failure for the whole SHPB system. Other future work includes performing the study in three-dimensional and in irregular (random) or oblique waves. Moreover, additional experimental validation will be beneficial.

6 CONCLUSIONS

An integrated CFD+CSM approach has been presented to fully simulate the hydroelastic interaction between nonlinear ocean waves and a deformable SHPB device. The feasibility and accuracy of this new approach have been validated against a series of previous experiments. Based on the validated model, a novel study has been conducted on the effect of the structural deformation of an SHPB on its wave damping performance. This study has shown that a deformable SHPB can have an evidently better wave damping performance than a rigid one.

However, the wave damping performance is quite sensitive to the SHPB's bending stiffness: The plate can be too stiff to show the FSI effect, or too flexible that performs a compliant behavior to the waves; in either of the situations, a large portion of the wave energy can still pass, which results in an unideal wave damping performance. Thereby, systematic simulations have been conducted to work out the optimal condition for an SHPB in a regular-wave condition, through varying the elasticity and aspect ratio of the device and investigating the corresponding wave damping performance. The derived optimal condition states the SHPB to vibrate at an amplitude that is close to the incident wave amplitude, leading to a resonant behavior that can damp the majority of the wave energy.

Based on the above achievements, two major contributions of the paper are summarized: (a) the present work has demonstrated a valid computer-aided approach that can perform hydroelastic offshore and coastal designs, which provides a significant advancement than previous methods based on the rigid-structure assumption; (b) the present work has for the first time demonstrated a hydroelastic design methodology for coastal breakwaters and showed that the deformation of the structure has a significant effect on the wave-damping performance.

As for the present hydroelastic CFD+CSM approach, it can also be used to simulate other deformable marine structures in waves or currents, such as to predict the deformations of large offshore platforms, bridges, wind turbines, and their corresponding influences on the surrounding wave field. Similarly, the method can be used to model wave energy converters that are based on a deforming mechanism, e.g. the bulge type (Chaplin, Heller, Farley, Hearn, & Rainey, 2012). As demonstrated, this two-way fully coupled approach allows the process of fluid-structure interaction to be simulated dynamically, manifesting the transient flow field whilst the structure is deforming. This is expected to be a great improvement to contemporary design approaches used in the coastal and offshore industries.

APPENDIX A: CFD EQUATIONS

The fluid sub-region is governed by the Navier-Stokes equations for incompressible, isothermal and Newtonian flow, as expressed in Equations (A1) and (A2).

$$\nabla \cdot \boldsymbol{v} = 0 \tag{A1}$$

$$\frac{\partial(\rho v)}{\partial \mathrm{t}} + \nabla \cdot (\rho \boldsymbol{v}\boldsymbol{v}) = -\nabla P + \nabla \cdot \tau + \rho g \tag{A2}$$

where $\boldsymbol{v}$ is velocity vector, P is pressure, ρ is the density and $\boldsymbol{\tau} = \mu(\nabla \boldsymbol{v} + \nabla \boldsymbol{v}^T)$ is the viscous stress in which μ is the dynamic viscosity, and g is the gravitational acceleration set at 9.81 m/s^2.

The VOF method is used to capture the free surface between air and water. The VOF method introduces a passive scalar field α, which denotes the fractional volume of a cell occupied by a specific phase. In this model, a value of $\alpha = 1$ corresponds to a cell full of water and a value of $\alpha = 0$ indicates a cell full of air. Thus, the free surface, which is a mix of these two phases, is formed by the cells with $0 < \alpha < 1$. The velocity of a free-surface cell is calculated based on the velocities of the nearest water cell and air cell, as expressed in Equation (A3) (Weller, 2002), and the evolution of free surface with time is solved by the advection equation of α, as expressed in Equation (A4) (Rusche, 2003). Furthermore, the local density and viscosity are determined according to Equations (A5) and (A6).

$$\boldsymbol{v} = \alpha \boldsymbol{v_{water}} + (1-\alpha)\boldsymbol{v_{air}} \tag{A3}$$

$$\frac{\partial \alpha}{\partial t} + \nabla \cdot (\boldsymbol{v}\alpha) + \nabla \cdot [\boldsymbol{v_r}\alpha(1-\alpha)] = 0 \tag{A4}$$

$$\rho = \alpha \rho_{water} + (1-\alpha)\rho_{air} \tag{A5}$$

$$\mu = \alpha \mu_{water} + (1-\alpha)\mu_{air} \tag{A6}$$

where $\boldsymbol{v_{water}}$ and $\boldsymbol{v_{air}}$ are the velocities of the nearest water cell and air cell respectively and $\boldsymbol{v_r} = \boldsymbol{v_{water}} - \boldsymbol{v_{air}}$ is the relative velocity between them (Vukčević, 2016). In this study, ρ_{water} = 1000 kg/m^3, μ_{water} = 1 × 10^{-3} N·s/m^2, ρ_{air} = 1 kg/m^3, and μ_{air} = 1.48 × 10^{-5} N·s/m^2. The VOF method can also be used for more than two phases, e.g. three phases; an example can be seen in Yaqub & Pendyala (2018), where the authors studied three phases of air, oil and water.

APPENDIX B: CSM EQUATIONS

The solid sub-region is governed by conservation of momentum, where the stress is given by the nonlinear St. Venant Kirchhoff hyperelastic law, as implemented in Cardiff, Karac, Jaeger, Jasak, Nagy, Ivankovic, & Tukovic (2018). The mathematical model in the total Lagrangian form (reference configuration) can be written as:

$$\oint \rho_{solid} \frac{\partial}{\partial t}\left(\frac{\partial \boldsymbol{u}}{\partial t}\right) dV = \oint \boldsymbol{n} \cdot (\Sigma \cdot \boldsymbol{F}^T)\, dS + \oint \rho_{solid} g\, dV \tag{B1}$$

where $\boldsymbol{u}$ is the displacement vector, and $\boldsymbol{F}$ = I + $(\nabla \boldsymbol{u})^{\mathrm{T}}$ is the deformation gradient tensor, and I is the second-order identity tensor and Σ is the second Piola-Kirchhoff stress tensor, which is related to the Cauchy stress tensor σ through Equation (B2).

$$\sigma = \frac{1}{\det \mathbf{F}} \boldsymbol{F} \cdot \Sigma \cdot \boldsymbol{F}^T \tag{B2}$$

The stress/strain relationship of the SHPB is dictated as below,

$$\Sigma = 2G\boldsymbol{S} + \Lambda\, tr(\boldsymbol{S})\boldsymbol{I} \tag{B3}$$

where the Green-Lagrange strain tensor is $\mathbf{S} = \frac{1}{2}[\nabla \mathbf{u} + (\nabla \mathbf{u})^{\mathrm{T}} + \nabla \mathbf{u} \cdot (\nabla \mathbf{u})^{\mathrm{T}}]$, and G and Λ are the Lamé's coefficients, related to the material properties of Young's modulus E and Poisson's ratio υ, as:

$$G = \frac{E}{2(1+\upsilon)} \quad \text{(B4)}$$

$$\Lambda = \frac{\upsilon E}{(1+\upsilon)(1-2\upsilon)} \quad \text{(B5)}$$

APPENDIX C: VERIFICATION OF THE FSI APPROACH AGAINST A BENCHMARK

Verification of the present CFD+CSM approach has been conducted against the famous FSI benchmark case proposed by Turek & Hron (2006). The case was named "FSI3" in the reference. Since the full description is lengthy, only the most salient points are given here.

The computational domain is divided into two parts, as shown in Figure C1, in which blue denotes the fluid mesh and red denotes the solid mesh. From the left boundary, a parabolic velocity profile is generated and moving towards the right. The flow interacts with a rigid cylinder structure (shown as the white circle in Figure C1), which generates a vortex-induced vibration for the elastic long beam. The velocity profile of the flow and the vortex-induced vibration are displayed in Figure C2. It can be seen that the flow field dynamically changes with the deformed slender structure (comparing subfigures (a) and (b)), indicating a two-way coupling of FSI is used in the present approach.

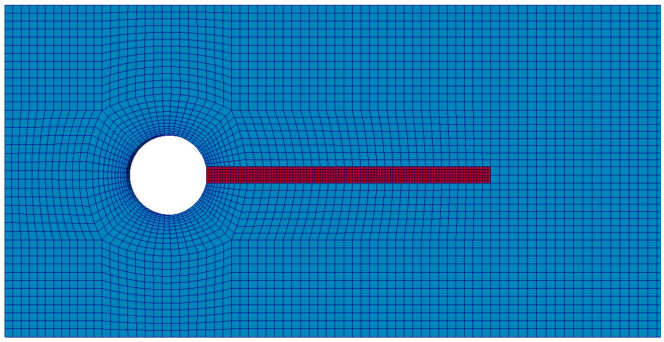

FIGURE C1. Mesh setup for the verification case.

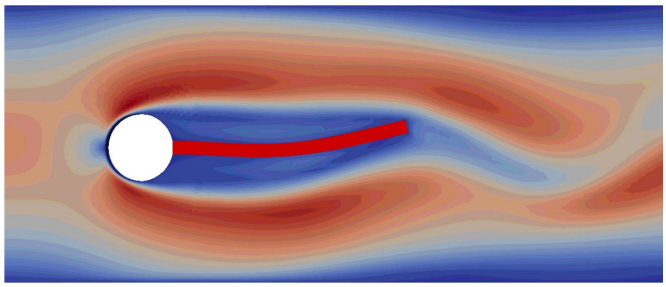

(a) Upwards deformation

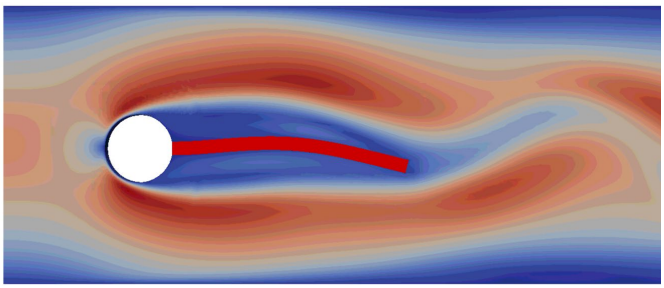

(b) Downwards deformation

FIGURE C2. Screenshots of the simulation.

The displacement of the middle point of the beam tail is measured and compared with the benchmark data, where the calculation using the present approach shows almost identical results as in the benchmark Figures on Page 259 of Turek & Hron (2006), which verifies the present FSI approach very well.

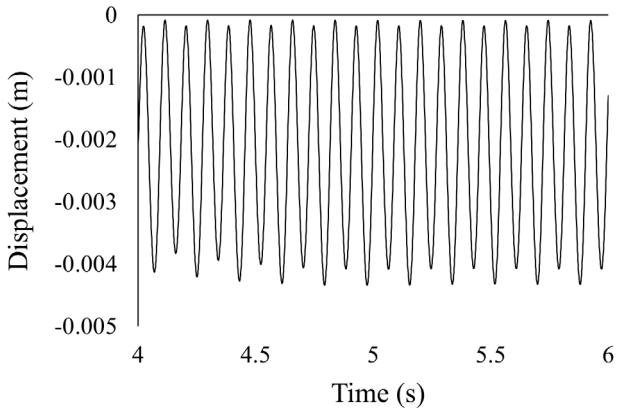

(a) Displacement in the horizontal direction

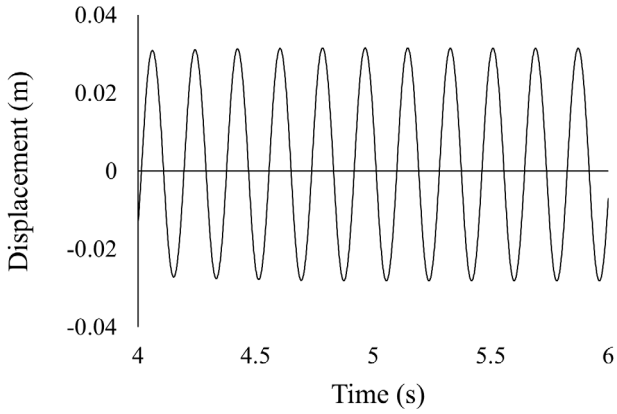

(b) Displacement in the vertical direction

FIGURE C3. Numerical results of the displacement for the middle point of the tail using the present CFD+CSM model.

ACKNOWLEDGMENTS

The authors would like to thank the Editor-in-Chief Prof Hojjat Adeli, the Guest Editors Prof Nicholas Fantuzzi, Prof Demosthenes Polyzos, Prof Dimitrios Pavlou, and seven anonymous reviewers for their constructive comments and valuable suggestions to improve the quality of the article. The second author acknowledges the funding from the European Union's Horizon 2020 research and innovation programme under the Marie Sklodowska-Curie grant agreement no. 713683 (COFUNDfellowsDTU).

REFERENCES

Adeli, H., & Kim, H. (2004). Wavelet-hybrid feedback-least mean square algorithm for robust control of structures. *Journal of Structural Engineering*, 130(1), 128–137.

Amezquita-Sanchez, J. P., & Adeli, H. (2015a). A new music-empirical wavelet transform methodology for time–frequency analysis of noisy nonlinear and non-stationary signals. *Digital Signal Processing*, 45, 55–68.

Amezquita-Sanchez, J. P., & Adeli, H. (2015b). Synchrosqueezed wavelet transform-fractality model for locating, detecting, and

quantifying damage in smart highrise building structures. *Smart Materials and Structures*, 24(6), 065034.

Amezquita-Sanchez, J. P., Park, H. S., & Adeli, H. (2017). A novel methodology for modal parameters identification of large smart structures using MUSIC, empirical wavelet transform, and Hilbert transform. *Engineering Structures*, 147, 148–159.

Anderlini, E. (2018). Control of wave energy converters using machine learning strategies [PhD Thesis]. University of Edinburgh.

Burke, J. E. (1964). Scattering of surface waves on an infinitely deep fluid. *Journal of Mathematical Physics*, 5(6), 805–819.

Cardiff, P., Karač, A., De Jaeger, P., Jasak, H., Nagy, J., Ivanković, A., & Tuković, Ž. (2018). An open-source finite volume toolbox for solid mechanics and fluid-solid interaction simulations. *ArXiv Preprint* ArXiv:1808.10736.

Celli, D., Li, Y., Ong, M. C., & Di Risio, M. (2019). The role of submerged berms on the momentary liquefaction around conventional rubble mound breakwaters. *Applied Ocean Research*, 85, 1–11.

Chaplin, J. R., Heller, V., Farley, F. J. M., Hearn, G. E., & Rainey, R. C. T. (2012). Laboratory testing the Anaconda. *Philosophical Transactions of the Royal Society A: Mathematical, Physical and Engineering Sciences*, 370(1959), 403–424.

Connell, K. O., & Cashman, A. (2016). Development of a numerical wave tank with reduced discretization error. 2016 *International Conference on Electrical, Electronics, and Optimization Techniques (ICEEOT)*, 3008–3012.

Coutand, D., & Shkoller, S. (2005). Motion of an elastic solid inside an incompressible viscous fluid. *Archive for Rational Mechanics and Analysis*, 176(1), 25–102.

del Carre, A., Muñoz-Simón, A., Goizueta, N., & Palacios, R. (2019). SHARPy: A dynamic aeroelastic simulation toolbox for very flexible aircraft and wind turbines. *Journal of Open Source Software*, 4(44), 1885.

Di Domenico, N., Groth, C., Wade, A., Berg, T., & Biancolini, M. E. (2018). Fluid structure interaction analysis: Vortex shedding induced vibrations. Procedia Structural Integrity, 8, 422–432.

Engineering Toolbox. (2003). Young's Modulus—Tensile and Yield Strength for common Materials. [online].

Fu, D., Zhao, X., Wang, S., & Yan, D. (2021). Numerical study on the wave dissipating performance of a submerged heaving plate breakwater. *Ocean Engineering*, 219, 108310.

Graw, K.-U. (1993). The Submerged Plate as a Wave Filter The Stability of the Pulsating Flow Phenomenon. *Coastal Engineering* 1992 (pp. 1153–1160).

Greene, T. R., & Heins, A. E. (1953). Water waves over a channel of infinite depth. *Quarterly of Applied Mathematics*, 11(2), 201–214.

Groth, C., Cella, U., Costa, E., & Biancolini, M. E. (2019). Fast high fidelity CFD/CSM fluid structure interaction using RBF mesh morphing and modal superposition method. *Aircraft Engineering and Aerospace Technology*.

He, M., Gao, X., Xu, W., Ren, B., & Wang, H. (2019). Potential application of submerged horizontal plate as a wave energy breakwater: A 2D study using the WCSPH method. *Ocean Engineering*, 185, 27–46.

He, M., Xu, W., Gao, X., & Ren, B. (2018a). SPH simulation of wave scattering by a heaving submerged horizontal plate. *International Journal of Ocean and Coastal Engineering*, 1(02), 1840004.

He, M., Xu, W., Gao, X., & Ren, B. (2018b). The layout of submerged horizontal plate breakwater (SHPB) with respect to the tidal-level variation. *Coastal Engineering Journal*, 60(3), 280–298.

Heins, A. E. (1950). Water waves over a channel of finite depth with a submerged plane barrier. *Canadian Journal of Mathematics*, 2, 210–222.

Huang, L. (2018). An opensource solver for wave-induced FSI problems. *In Proceedings of CFD with OpenSource Software*. Edited by Nilsson. H. http://dx.doi.org/10.17196/OS_CFD#YEAR_2017

Huang, L., Ren, K., Li, M., Tuković, Ž., Cardiff, P., & Thomas, G. (2019). Fluid-structure interaction of a large ice sheet in waves. *Ocean Engineering*, 182, 102–111.

Huang, X., & Kwon, O.-S. (2020). An integrated simulation method for coupled dynamic systems. *Computer-Aided Civil and Infrastructure Engineering.*

Ijima, T., Ozaki, S., Eguchi, Y., & Kobayashi, A. (1970). Breakwater and quay well by horizontal plates. *Coastal Engineering* 1970 (pp. 1537–1556).

Jacobsen, N. G., Fuhrman, D. R., & Fredsøe, J. (2012). A wave generation toolbox for the open-source CFD library: OpenFOAM®. *International Journal for Numerical Methods in Fluids*, 70(9), 1073–1088.

Kim, H., & Adeli, H. (2005). Wavelet-hybrid feedback linear mean squared algorithm for robust control of cable-stayed bridges. *Journal of Bridge Engineering*, 10(2), 116–123.

Li, Y., Ong, M. C., & Tang, T. (2020). A numerical toolbox for wave-induced seabed response analysis around marine structures in the OpenFOAM® framework. *Ocean Engineering*, 195, 106678.

Li, Y., Ong, M. C., & Tang, T. (2018). Numerical analysis of wave-induced poro-elastic seabed response around a hexagonal gravity-based offshore foundation. *Coastal Engineering*, 136, 81–95.

Liu, C., Huang, Z., & Tan, S. K. (2009). Nonlinear scattering of non-breaking waves by a submerged horizontal plate: Experiments and simulations. *Ocean Engineering*, 36(17–18), 1332–1345.

Liu, P. L.-F., & Iskandarani, M. (1991). Scattering of short-wave groups by submerged horizontal plate. *Journal of Waterway, Port, Coastal, and Ocean Engineering*, 117(3), 235–246.

Masoomi, M., & Mosavi, A. (2021). The One-way FSI method based on RANS-FEM for the Open Water Test of a Marine propeller at the different advance coefficient. *Preprints*.

McVicar, J., Lavroff, J., Davis, M. R., & Thomas, G. (2018). Fluid–structure interaction simulation of slam-induced bending in large high-speed wave-piercing catamarans. *Journal of Fluids and Structures*, 82, 35–58.

Meylan M., Bennetts, L., Cavaliere, C., Alberello, A., & Toffoli, A. (2015). Experimental and theoretical models of wave-induced flexure of a sea ice floe. *Physics of Fluids*, 27(4).

Meylan, M. H. (2021). Time-Dependent Motion of a Floating Circular Elastic Plate. *Fluids*, 6(1), 29.

Mohapatra, S. C., & Sahoo, T. (2014). Wave interaction with a floating and submerged elastic plate system. *Journal of Engineering Mathematics*, 87(1), 47–71.

Muha, B., & Canić, S. (2013). Existence of a weak solution to a nonlinear fluid–structure interaction problem modeling the flow of an incompressible, viscous fluid in a cylinder with deformable walls. *Archive for Rational Mechanics and Analysis*, 207(3), 919–968.

Okubo, H., Takahashi, Y., Kojima, I., & Moritaka, H. (1994). Development of New Types of Breakwaters (Nippon Steel Technical Report No. 60).

Park, K., Kim, H., & Kim, D.-J. (2019). Generalized finite element formulation of fiber beam elements for distributed plasticity in multiple regions. *Computer-Aided Civil and Infrastructure Engineering*, 34(2), 146–163.

Patarapanich, M. (1984). Maximum and zero reflection from submerged plate. *Journal of Waterway, Port, Coastal, and Ocean Engineering*, 110(2), 171–181.

Peng, Q., & Yi-Jun, H. (2003). Numerical wave flume study on wave motion around submerged plates. *China Ocean Engineering*, 17(3), 397–406.

Perez-Ramirez, C. A., Amezquita-Sanchez, J. P., Adeli, H., Valtierra-Rodriguez, M., Camarena-Martinez, D., & Romero-Troncoso, R. J. (2016). New methodology for modal parameters identification of smart civil structures using ambient vibrations and synchrosqueezed wavelet transform. *Engineering Applications of Artificial Intelligence*, 48, 1–12.

Rusche, H. (2003). Computational fluid dynamics of dispersed two-phase flows at high phase fractions [PhD Thesis]. Imperial College London (University of London).

Siew, P. F., & Hurley, D. G. (1977). Long surface waves incident on a submerged horizontal plate. *Journal of Fluid Mechanics*, 83(1), 141–151.

Sree, D. K., Law, A. W.-K., & Shen, H. H. (2017). An experimental study on the interactions between surface waves and floating viscoelastic covers. *Wave Motion*, 70, 195–208.

Sumer, B. M., & Fredsøe. (2006). Hydrodynamics around cylindrical strucures (Vol. 26). World scientific.

Sumer, B. M., & Fredsøe, J. (2000). Experimental study of 2D scour and its protection at a rubble-mound breakwater. *Coastal Engineering*, 40(1), 59–87.

Tukovic, Z., Cardiff, P., Karac, A., Jasak, H., & Ivankovic, A. (2014). OpenFOAM library for fluid structure interaction. *9th OpenFOAM Workshop*, 2014.

Tuković, Ž., Karač, A., Cardiff, P., Jasak, H., & Ivanković, A. (2018). OpenFOAM Finite Volume Solver for Fluid-Solid Interaction. *Transactions of FAMENA*, 42(3), 1–31. https://doi.org/10.21278/TOF.42301

Turek, S., & Hron, J. (2006). Proposal for numerical benchmarking of fluid-structure interaction between an elastic object and laminar incompressible flow. *Fluid-structure interaction* (pp. 371–385). Springer.

van Loon, R., Anderson, P. D., van de Vosse, F. N., & Sherwin, S. J. (2007). Comparison of various fluid–structure interaction methods for deformable bodies. *Computers & Structures*, 85(11–14), 833–843.

Vukčević, V. (2016). Numerical modelling of coupled potential and viscous flow for marine applications. FAMENA Doctoral Thesis, Zagreb.

Wang, K.-H., & Shen, Q. (1999). Wave motion over a group of submerged horizontal plates. *International Journal of Engineering Science*, 37(6), 703–715.

Wang, Y. (2017). Research on submerged inclined-plate breakwater for wave control [Master's Thesis]. Tokyo University of Marine Science and Technology.

Weller, H. G. (2002). Derivation, modelling and solution of the conditionally averaged two-phase flow equations. In Technical Report TR/HGW/02. Nabla Ltd.

Yu, X. (2002). Functional performance of a submerged and essentially horizontal plate for offshore wave control: A review. *Coastal Engineering Journal*, 44(02), 127–147.

Yu, X., Isobe, M., & Watanabe, A. (1995). Wave breaking over submerged horizontal plate. *Journal of Waterway, Port, Coastal, and Ocean Engineering*, 121(2), 105–113.

Yaqub, M., & Pendyala, R. (2018). CFD simulations of gas-liquid-liquid three-phase co-current flow in horizontal pipe by tracking volume fractions using VOF model. *In IOP Conference Series: Materials Science and Engineering*, 458(1), 012078. IOP Publishing.

Zhou, Z., & Adeli, H. (2003). Time-frequency signal analysis of earthquake records using Mexican hat wavelets. *Computer-Aided Civil and Infrastructure Engineering*, 18(5), 379–389.

Zhu, Z., Gu, M., & Chen, Z. (2007). Wind tunnel and CFD study on identification of flutter derivatives of a long-span self-anchored suspension bridge. *Computer-Aided Civil and Infrastructure Engineering,* 22(8), 541–554.